ELSEVIER

Fuel 78 (1999) 1345–1362

FUEL

www.elsevier.com/locate/fuel

The effect of pore structure and gas pressure upon the transport properties of coal: a laboratory and modeling study. 2. Adsorption rate modeling

C.R. Clarkson[a,*], R.M. Bustin[b]

[a]*Burlington Resources, San Juan Division, 3535 E. 30th St. 87402-8801, P.O. Box 4289, Farmington, NM 87499-4289, USA*
[b]*Department of Earth and Ocean Sciences, The University of British Columbia, 6339 Stores Road, Vancouver, British Columbia V6T 1Z4, Canada*

Received 24 December 1997; received in revised form 9 February 1999

Abstract

The effect of coal composition, pore structure, and gas pressure upon methane and carbon dioxide gas transport in Cretaceous Gates Formation coal is investigated. Coal matrix gas transport models, which assume a homogeneous unimodal pore structure and linear adsorption isotherms, are not appropriate for modeling methane or carbon dioxide adsorption rates in all coal lithotypes.

model diffusivities, which are corrected for the effects of nonlinear adsorption, are larger than diffusivities obtained for analytical models for pore diffusion.

Methane and carbon dioxide gas analytical and numerical model effective diffusivities are sensitive to the starting pressure in an adsorption step. The pressure-dependence of the analytical solution diffusivities is likely due to the nonlinearity of the adsorption isotherm. The effect of gas pressure upon diffusivities, obtained from the numerical model, indicate that the mechanism of gaseous diffusion is bulk diffusion.

Results of the current study have important implications for coalbed methane reservoir characterization, the determination of gas contents for gas resource calculations, gas production simulations, and the prediction of outbursting in coal seams.

Keywords: Coal; Methane; Adsorption rate models

Nomenclature

C	sorbate concentration (kg/m^3)
D	diffusion coefficient (m^2/s)
D'	$D/r_p^2(\phi/(\phi + SH))$, apparent diffusivity (s^{-1})
g	micropore/macropore mass transfer term (kg/m^3)
H	Henry's law constant (m^3/m^2)
M	mass content (kg/m^3)
N	number of coal particles (macrospheres) in system
r	radius (m)
r_p	diffusion path length (m)
R_a	macrosphere or particle radius (m)
R_i	microsphere radius (m)
S	pore surface area per unit bulk volume of coal (m^2/m^3)
t	time (s)
V	volume (m^3), or volume adsorbed (cm^3/g at STP)

Subscripts

a	macropore
D	dimensionless
i	micropore
L	Langmuir
s	sorbate
v	voids

* Corresponding author. Tel.: + 1-505-326-9729; fax: + 1-505-599-4017.

E-mail address: cclarkson@br-inc.com (C.R. Clarkson)

0016-2361/99/$ - see front matter
PII: S0016-2361(99)00056-3

Greek symbols

α	$R_a^2 D_i / D_a R_i^2$, dimensionless parameter
β	$(3(1-\phi_a)\phi_i/\phi_a)(R_a^2 D_i / D_a R_i^2) = (3(1-\phi_a)\phi_i/\phi_a)$ α, dimensionless parameter
γ	r_i/R_i, dimensionless microsphere radial position
η	r_a/R_a, dimensionless macrosphere radial position
ϕ	porosity
ρ	gas density (kg/m^3)
τ	$D_a t/R_a^2$, dimensionless time

1. Introduction

Knowledge of the transport properties of coal is important for the accurate prediction of gas and water production rates from coal seams. The mechanisms of storage and transport of gas and water in coal seams differ significantly from conventional gas reservoirs. It is commonly assumed that gas transport in coal may be analysed at two scales: laminar flow through the macroscopic cleat, the natural fracture system of coal, and diffusion through the coal matrix bounded by cleat [1,2]. The flow through the cleat is pressure-driven and may be modeled using Darcy's Law, whereas flow through the matrix is assumed to be concentration-driven and is modeled using Fick's law. Significant gas storage, through the mechanism of physical adsorption, occurs mainly in the coal matrix, which acts as a source for gas production.

Recent modeling studies [3,4] have shown that adsorption time, which is dependent upon the coal matrix diffusion constant, has little effect upon long term gas production from coal seams, but has a marked effect upon short term production [4]. Gas transport through the coal seam fracture system, which is dependent upon relative permeability, is therefore considered to be a greater control upon long-term production. Production of gas from coal mine gob zones, on the other hand, may be more strongly controlled by the diffusional characteristics of the coal matrix [5].

Gas content determinations from conventional coal core often rely upon coal matrix gas transport modeling in order to obtain estimates of gas lost during core recovery [6]. For example, the Direct Method involves the solution of a partial differential equation describing isothermal diffusion following a step change in boundary concentration [6]. One of the main sources of error in determining diffusion coefficients and lost gas volumes is performing desorption at nonreservoir temperatures [7]. Further, the more gas that is lost during core recovery, the more difficult it is to accurately determine lost gas volumes and diffusivity.

The current study presents an experimental method and new numerical models for determining diffusivities from high-pressure methane and carbon dioxide adsorption/desorption volumetric isotherm data. The proposed method offers the advantage of simultaneous determination of the adsorption isotherm, from which the coal gas capacity can be determined, as well as adsorption rate data. These data may be obtained relatively rapidly as the experiments are performed on crushed coal particles. The isotherm data were used as input to new numerical models, which are developed and tested for coals of varying pore volume distribution and adsorption characteristics. Coals of varying lithotype composition were chosen for this study as it is known that coal composition has an important control upon pore volume distributions [8,9] and gas adsorption characteristics [10–12]. Although Mavor et al. [13] obtained diffusion coefficients from adsorption isotherm data, the model proposed was not adequate for use at all pressure steps of the isotherm, or for coals with heterogenous pore structure.

Few studies [14,15] have reported experimentally determined carbon dioxide diffusion parameters in coal even though carbon dioxide may be a significant component in coalbed gas [16]. In the current study, carbon dioxide adsorption rate data are reported and modeled under a variety of temperature and pressure conditions for Gates Formation coals in order to assess the factors controlling carbon dioxide coal matrix transport. This information may be important for the accurate evaluation of carbon dioxide injection strategies for the enhanced recovery of coalbed methane [17].

The method proposed here provides an alternative to gas canister desorption data for the determination of matrix transport parameters if these data are not available.

2. Background

The conventional approach to modeling matrix gas transport is the application of the unipore diffusion model to transient volumetric [18–20] or gravimetric [21] adsorption or desorption data. The unipore model is based upon the solution to Fick's second law for spherically symmetric flow:

$$\frac{D}{r^2}\frac{\partial}{\partial r}\left(r^2\frac{\partial C}{\partial r}\right) =$$

where r is the ra… diffusion coeffici… tion assumes that… concentration an…

1. isothermal co…
2. homogenous p…

The solution to… the diffusing spe…

$$\frac{M_t}{M_\infty} = 1 - \frac{6}{\pi^2}$$

where M_t is the to… that has left the p… desorbed mass, a… tionship may be …

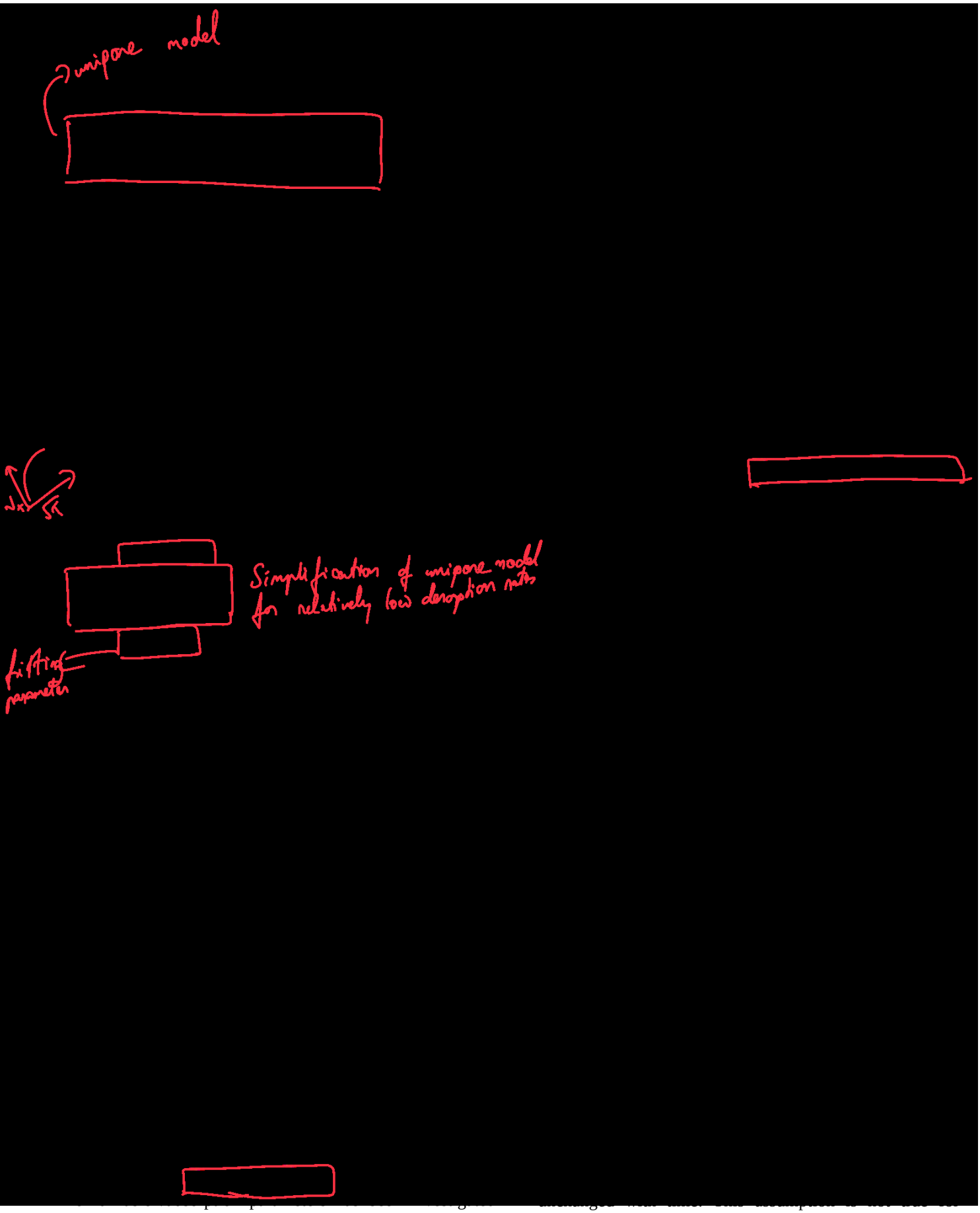

using a single parameter (effective diffusivity) diffusion/ adsorption model [26] for single porous particles of various geometric shapes. Smith and Keller [26] noted that for sphe-

constant volume, variable pressure adsorption rate experiments as described by Mavor et al. [13], or as utilized here. Secondly, methane and carbon dioxide adsorption isotherms

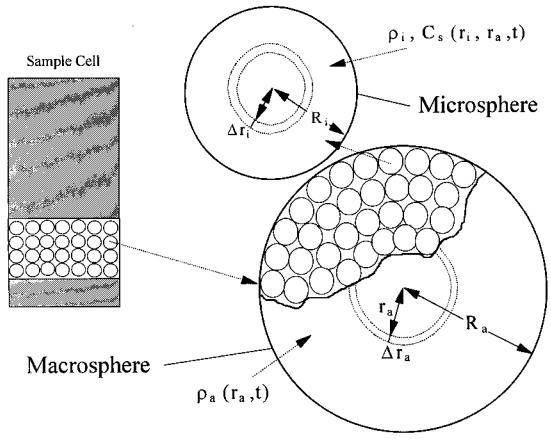

Fig. 1. Conceptual model for bidisperse pore structure. The time- and space-dependent variables in the macro- and microspheres are indicated.

for bituminous coal are known to be nonlinear, and the application of linear adsorption models, is inadequate for most coals.

3. Methods

3.1. Adsorption rate analysis

Adsorption rate data were collected during high-pressure methane and carbon dioxide adsorption isotherm analysis [redacted] computer-controlled adsorption analysis, pressure data in the sample cell were collected at 1 s intervals for the first 300 s and then at increasing intervals (10, 60, and finally 3000 s) until equilibrium was achieved. Pressures were then converted to real gas densities using the Real Gas Law. Desorption analyses were performed manually following the same procedure as adsorption analysis. Pressure data were collected every 100 s.

One of the main problems with the variable pressure, constant volume adsorption technique is that time is required to attain thermal equilibrium in the cell after the gas has been adiabatically compressed into the cell. Thus, the first few seconds of adsorption data are unusable. To determine the length of time required to cool back to the water bath temperature, an empty sample cell was filled with steel balls having a similar total solid volume as the coals used. An isotherm analysis at the same pressure steps as the coal samples was then performed to determine the length of time required for the pressure to drop due to re-equilibration with bath temperature. For the low-pressure steps, this time was less than 10 s, but became longer as the pressure was increased. This translates into an initial short time period where negative values of volume adsorbed are calculated. The "clock" was therefore started where the volume adsorbed passed through a value of zero.

Volume adsorbed and time data were also collected using an ASAP 2010® volumetric gas apparatus during low-pressure (273 K) carbon dioxide isotherm collection. In this case, data were collected in 5 s increments for a total of 5000 s.

3.2. Isotherm and adsorption rate model

The Langmuir isotherm equation [33] was used to model equilibrium high-pressure gas sorption data for the dry and wet coals. The equation may be expressed for plotting purposes as:

$$\frac{P}{V} = \frac{P}{V_L} + \frac{P_L}{V_L}. \tag{6}$$

A linear regression is performed for P/V vs. P plots to obtain the Langmuir constants.

The adsorption rate model used in the current study assumes a bidisperse pore structure for coal (Fig. 1), similar to the Ruckenstein [28] model. The Ruckenstein model assumes that the pore structure is bimodal and that the adsorbent particle contains uniform radius (nonoverlapping) microporous microspheres with the space between microspheres making up the macroporosity. The Ruckenstein model [28] also assumes linear isotherms in both macroporosity and microporosity and a step change in boundary [redacted] current model may be summarized as follows:

1. Isothermal system.
2. Applicable transport equation is Fick's first law: $F = -D\nabla(\phi\rho)$, where F = mass flux (kg/m s), D = diffusion coefficient (m^2/s), ϕ is the porosity and ρ the gas phase density.
3. Gas phase densities can be expressed using the Real Gas Law: $\rho = MP/zRT$, where M is the molecular weight of the gas (kg/mole), P the gas pressure (Pascals), z the compressibility factor and R the universal gas constant (J/mol K).
4. Transport mechanism is diffusion in both macro- and micropores.
5. Significant adsorption occurs only in the microporosity and the adsorption isotherm can be described by the Langmuir equation.
6. Pores are incompressible.
7. Void volume is constant with time. No correction is made for void volume shrinkage during adsorption of gas.
8. The gas phase is mobile whereas the adsorbed phase is immobile.

9. Coal particles are spherical in shape and uniform in size.

The macropore (7) and micropore (8) transport equations use

tration in microporosity is uniform for all microspheres (Eq. (10)). A no (free gas) flow internal boundary condition is used for the macrospheres and microspheres (Eqs. (11) and (12)). Eq. (13) is a mass balance statement which expresses that the change in mass of gas stored in the interparticle void space is equal to the mass flux of gas across all (assumed spherical) particle (equal radius) boundaries for $t > 0$. Eq. (14) states that the gas density at the microsphere boundary is equal to the gas density in the macroporosity at r_a.

Introducing the dimensionless variables and parameters:

$$\rho_D = \frac{\rho}{\rho_o}, \qquad \gamma = \frac{r_i}{R_i}, \qquad \eta = \frac{r_a}{R_a}, \qquad \tau = \frac{D_a t}{R_a^2},$$

$$\alpha = \frac{R_a^2 D_i}{D_a R_i^2}, \quad \beta = \frac{3(1-\phi_a)\phi_i}{\phi_a}\frac{R_a^2 D_i}{D_a R_i^2} = \frac{3(1-\phi_a)\phi_i}{\phi_a}\alpha.$$

Eqs. (7) and (8) become:

$$\frac{1}{\eta^2}\frac{\partial}{\partial\eta}\left(\eta^2\frac{\partial\rho_{D_a}}{\partial\eta}\right) = \frac{\partial\rho_{D_a}}{\partial\tau} + \beta\frac{\partial\rho_{D_i}}{\partial\gamma}\Big|_{\gamma=1}, \tag{15}$$

$$\frac{\alpha}{\gamma^2}\frac{\partial}{\partial\gamma}\left(\gamma^2\frac{\partial\rho_{D_i}}{\partial\gamma}\right) = \frac{\partial}{\partial\tau}\left(\rho_{D_i} + \frac{C_s}{\rho_o\phi_i}\right) \tag{16}$$

with initial conditions:

$$\rho_{D_a}(0,\eta) = \rho_{D_o} = \rho_{D_i}(0,\gamma), \tag{17}$$

with initial conditions:

$$\rho_{D_o} = \rho_{D_i}(0,\gamma), \tag{24}$$

$$C_s(0,\gamma) = C_{so} \tag{25}$$

and boundary conditions:

$$\frac{\partial\rho_{D_i}}{\partial\gamma} = 0 \qquad \text{at } (\tau,0), \tag{26}$$

$$V_v\frac{\partial\rho_{D_i}}{\partial\tau} = -N4\pi R_a^3\phi\frac{\partial\rho_{D_i}}{\partial\gamma}\Big|_{\gamma=1} \qquad \text{at } (\tau,1), \tag{27}$$

where $\tau = D_i t/R_a^2$ and $\gamma = r_i/R_a$.

For the numerical models, the Langmuir equation is cast in the following dimensionless form:

$$\frac{\rho_D}{C_S} = \frac{\rho_{DL}}{C_S} + \frac{\rho_D}{C_{SL}},$$

where ρ_D is the dimensionless external gas density, ρ_{D_L} is the Langmuir dimensionless gas density, analogous to the Langmuir pressure, and C_{SL} is the mass sorbed at infinite pressure. As with the Langmuir equation (6),

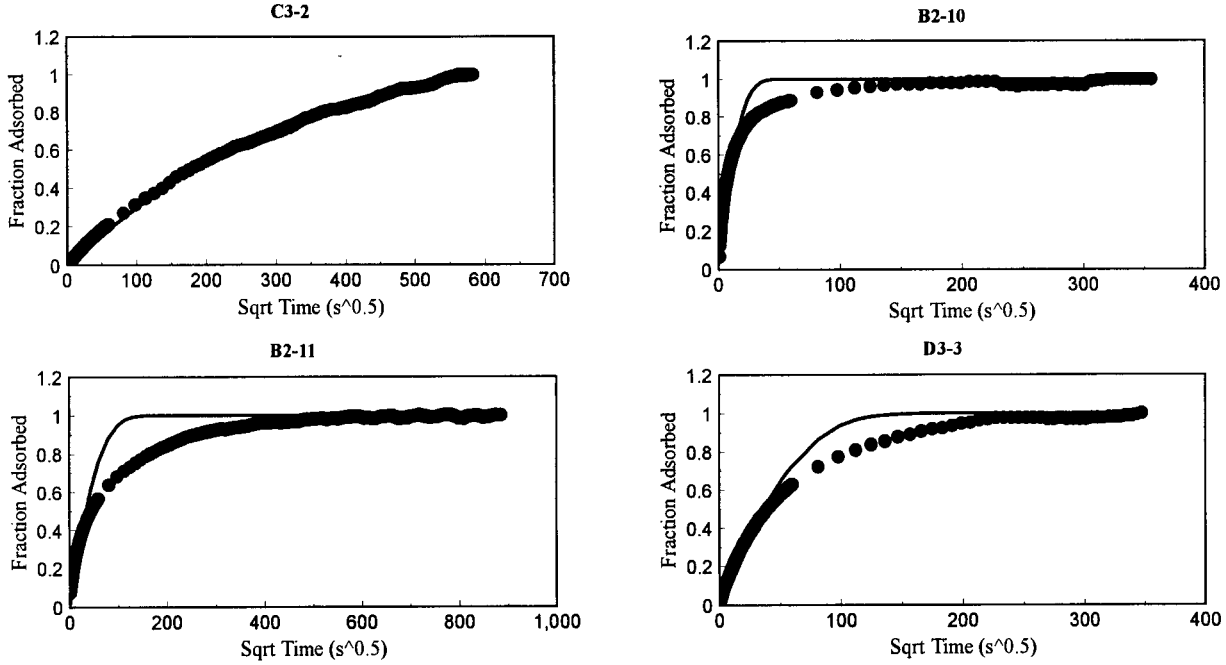

Fig. 2. Unipore analytical model fit to − 4 mesh (dry) coal methane adsorption rate data.

a linear regression is performed for plots of ρ_D/C_S vs. ρ_D.

The unipore numerical solution, programmed in FORTRAN, was verified against analytical solutions for spherical diffusion presented in Crank [22]. The bidisperse numerical solution, also programmed in FORTRAN, was verified against the analytical solution (Eq. (11)) presented in Ruckenstein et al. [28].

A least-squares criterion was used to fit the model to the experimental gas density data. For the unipore model, the effective diffusivity (D_i/R_a^2) was adjusted to minimize the least-squares function, using the Golden Section Search

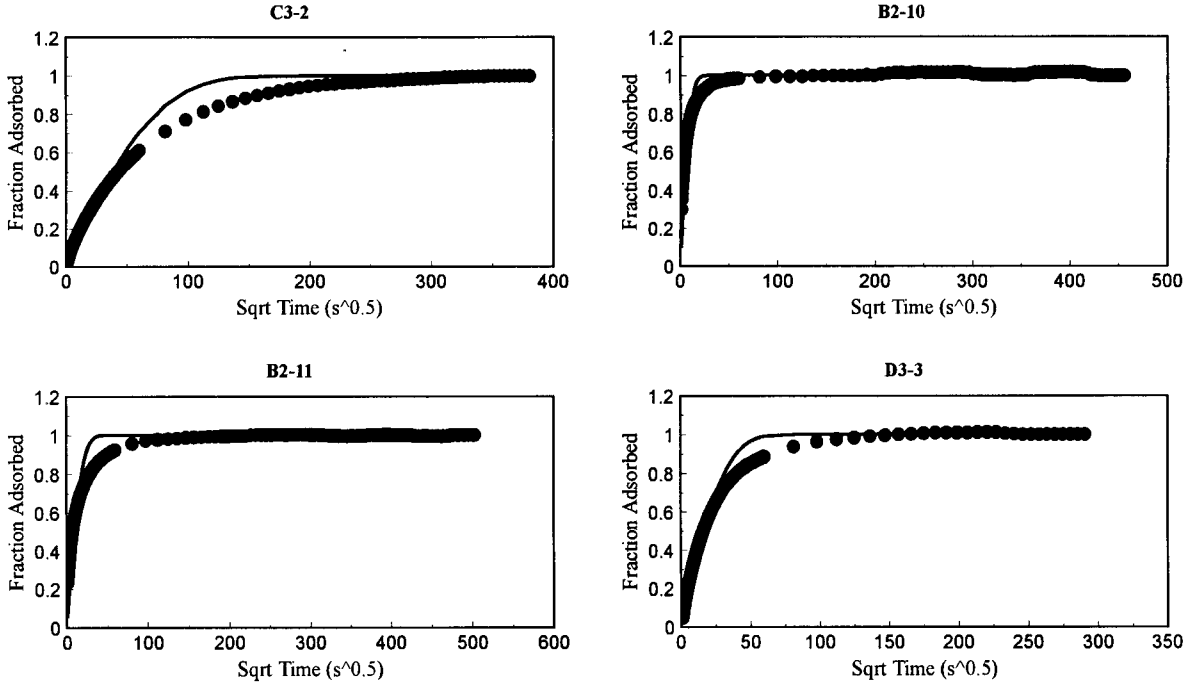

Fig. 3. Unipore analytical model fit to − 4 mesh (dry) coal carbon dioxide methane adsorption rate data.

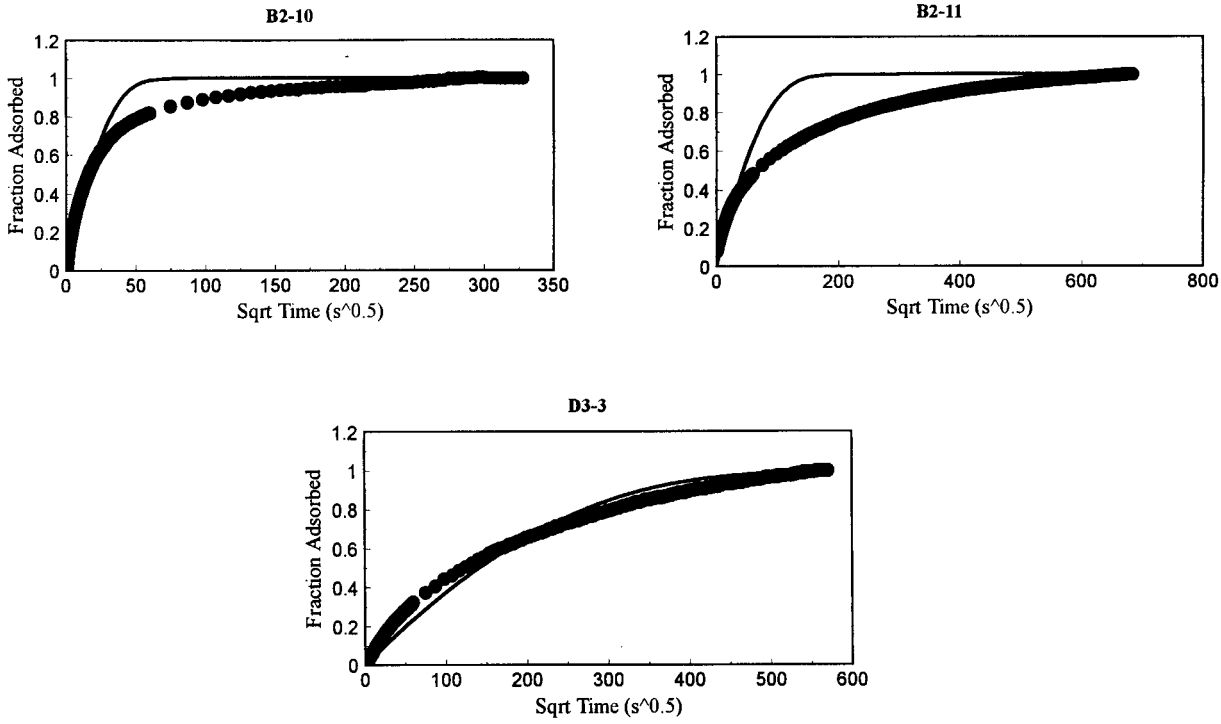

Fig. 4. Unipore analytical model fit to − 4 mesh (wet) coal methane adsorption rate data.

algorithm [36]. The bidisperse numerical model parameters ($D_a/R_a^2, \alpha, \beta$) were optimized using the Downhill Simplex Method algorithm [36]. The least-squares function utilized is:

$$L = \sum_{i=1}^{NP} \left(\rho_{exp,i} - \rho_{calc,i}\right)^2$$

where ρ_{exp}, and ρ_{calc} are the experimentally determined and calculated gas densities, respectively, external to the coal particles. Typically 3000–10 000 timesteps were taken with the numerical model, and the model densities at each experimental real time step were determined from interpolation.

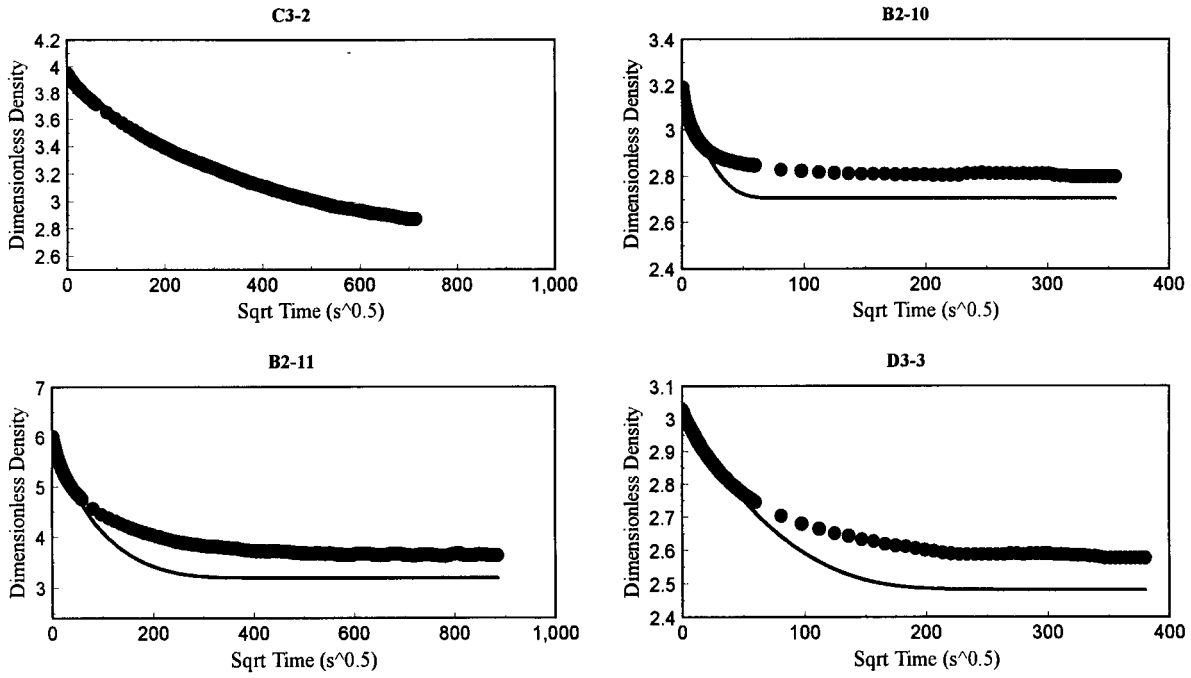

Fig. 5. Unipore numerical model fit to − 4 mesh (dry) coal methane adsorption rate data.

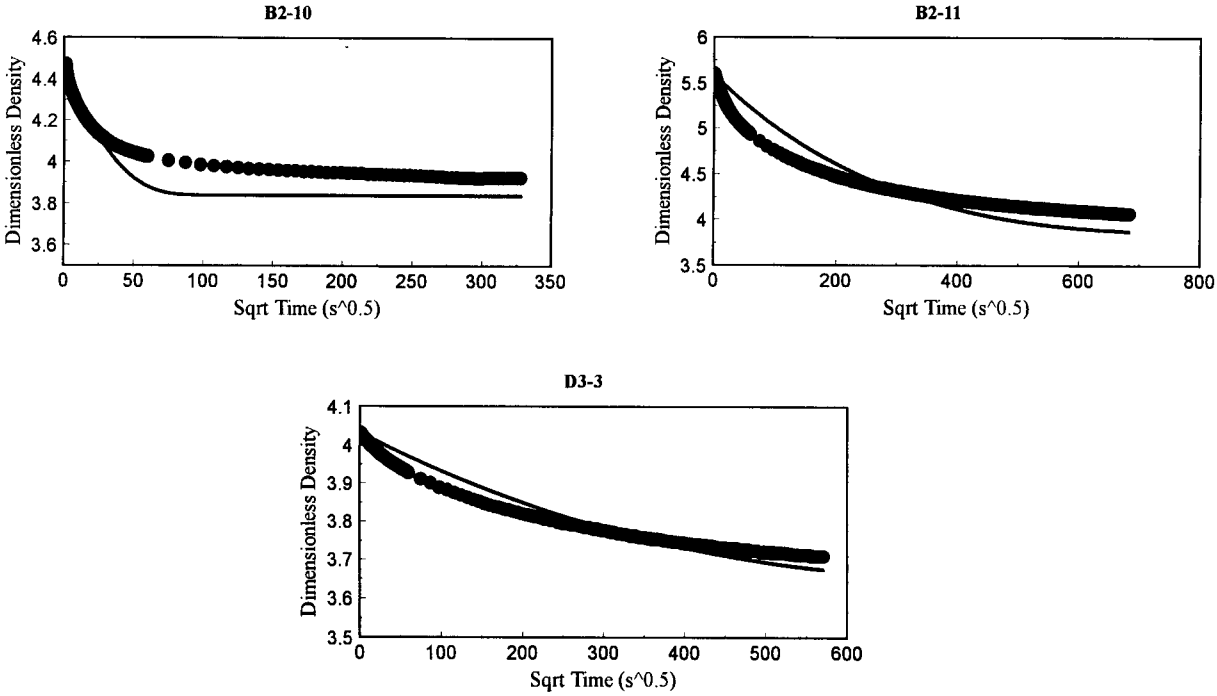

Fig. 6. Unipore numerical model fit to − 4 mesh (wet) coal methane adsorption rate data.

4. Results and discussion

4.1. High-pressure methane and carbon dioxide adsorption rate data: application of unipore models

High-pressure methane and carbon dioxide adsorption rate data (adsorption isotherm pressure step 2) on dry and moisture-equilibrated coal has been modeled using the unipore analytical model (Eq. (3)) (Figs. 2–4) and the current numerical model (Eqs. (23)–(27)) (Figs. 5–7).

The best-fit effective diffusivities (D') (Table 1) for the analytical solution are apparent diffusivities that do not include nonlinear isotherm effects. The apparent diffusivity for the unipore pore diffusion analytical solution, which

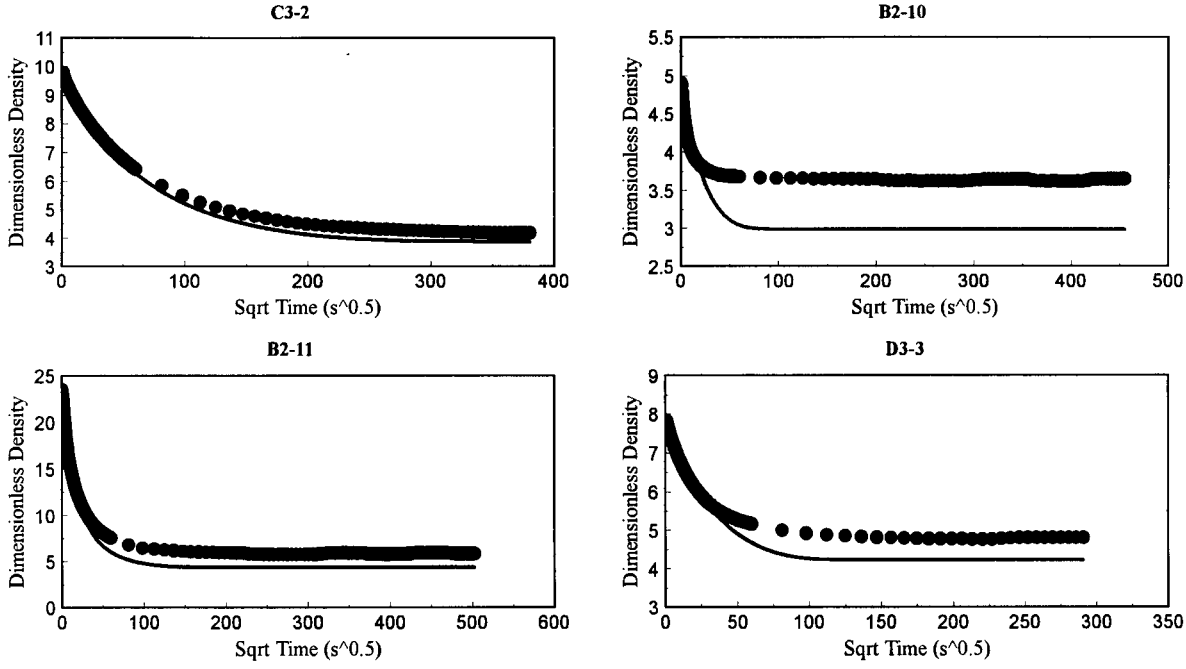

Fig. 7. Unipore numerical model fit to − 4 mesh (dry) coal carbon dioxide adsorption rate data.

Table 1
Unipore analytical model parameters for adsorption rate data-isotherm pressure step 2

Sample	CH_4 on dry coal		CH_4 on moisture-equilibrated coal		CO_2 on dry coal	
	P (MPa)	D'^a (s^{-1})	P (MPa)	D' (s^{-1})	P (MPa)	D' (s^{-1})
C3-2	0.9	7×10^{-7}	–	–	0.3	2×10^{-5}
B2-11	0.8	3×10^{-5}	1.5	2×10^{-5}	0.2	3×10^{-4}
D3-3	1.0	2×10^{-5}	1.9	2×10^{-6}	0.5	1×10^{-4}
B2-10	1.1	3×10^{-4}	1.8	1×10^{-4}	0.6	1×10^{-3}

[a] $D' = D/r_p^2(\phi/(\phi + SH))$.

assume linear adsorption on the pore walls, may be expressed as:

$$D' = \frac{D}{r_p^2}\left(\frac{\phi}{\phi + SH}\right).$$

Sample C3-2 (high vitrinite/low ash) has a smaller effective diffusivity value than all other coals. In addition, the unipore model provides a reasonable fit to methane adsorption rate data over the entire time range for only C3-2, whereas for all the other coals the unipore model significantly underestimates the time required to reach equilibrium. The unipore model also fails to adequately model the carbon dioxide adsorption rate data for sample C3-2.

Carbon dioxide diffusivities for dry coals obtained in this study are significantly larger than for the methane diffusivities (up to ~28 times), although direct comparison is difficult, due to the difference in final equilibrium pressure for methane and carbon dioxide isotherms. In a study by Marecka [15], a similar ratio of carbon dioxide to methane effective diffusivities was found using the unipore analytical model for constant pressure adsorption (~2.5 kPa, 303 K).

Analytical model diffusivities for the wet coal data (Table 1) are smaller than for the dry coals. As with the dry coal data, the unipore analytical model does not provide an adequate fit to adsorption rate data over the entire time scale (Fig. 4). The possible exception, however, is sample D3-3. It is possible that water is occupying some of the larger pores of this sample, denying methane access to these pores, and hence the coal would be effectively unimodal with respect to pore volume distribution.

Results of the numerical model fit to the adsorption rate data are shown in Figs. 5–7, best-fit diffusivities are provided in Table 2 and numerical model input parameters are provided in Table 3. The numerical model diffusivities (D_i/R_a^2) are relatively insensitive to the value used for the estimate of the mean particle radius (Part 1). The unipore numerical model provides a reasonable fit only for sample C3-2. The poor fit for other samples may be due to the assumption of a unimodal pore volume distribution, error in the Langmuir equation fit to the adsorption isotherm data (as mentioned in Part 1) or errors in the porosity estimates. In addition, some curve fitting error results from the fact that time intervals for data collection were not evenly spaced, resulting in more pressure points taken at early time (see Section 3) than for later time. The greater number of data points at early time biases the curve fits toward the early time data.

The discrepancy in the magnitude of best-fit diffusivities between the analytical and numerical models (Tables 1 and 2) is likely due to two factors. Firstly, the (external) boundary conditions for the models are different in that the analytical model was developed for a step change in boundary concentration at $t = 0$, whereas a variable flux boundary condition was employed for the numerical model (Eq. (27)). Secondly, the numerical model accounts for nonlinear adsorption during gas transport.

The adsorption rate behaviour of the Gates coals may be explained in terms of the relative proportions of micro, meso, and macroporosity determined in Part 1. The slowly sorbing sample C3-2 has a relatively large micropore volume (0.049 cm^3/g) compared to D3-3 (0.025 cm^3/g) and B2-10 (0.025 cm^3/g). In addition, C3-2 has very little meso/macroporosity. The sample is homogenous with

Table 2
Unipore numerical model parameters for adsorption rate data-isotherm pressure step 2

Sample	CH_4 on dry coal		CH_4 on moisture-equilibrated coal		CO_2 on dry coal	
	P (MPa)	D_i/R_a^2 (s^{-1})	P (MPa)	D_i/R_a^2 (s^{-1})	P (MPa)	D_i/R_a^2 (s^{-1})
C3-2	0.9	1×10^{-5}	–	–	0.3	4×10^{-4}
B2-11	0.8	6×10^{-5}	1.5	6×10^{-6}	0.2	1×10^{-3}
D3-3	1.0	2×10^{-4}	1.9	7×10^{-6}	0.5	2×10^{-3}
B2-10	1.1	1×10^{-3}	1.8	5×10^{-4}	0.6	3×10^{-3}

Table 3
Input parameters for numerical models-isotherm pressure step 2

	Sample	C_{so} (kg/m^3)	ρ_o (kg/m^3)	ρ_I[a] (kg/m^3)	S_L[b]	I_L[b]	N	ϕ[c]	ϕ_i[c]	V_v (m^3 × 10^4)
CH_4 (dry coal)										
	C3-2	3.361	2.481	8.214	0.0554	0.242	2181	0.028	–	1.107
	B2-11	3.296	1.393	8.342	0.0546	0.249	2783	0.056	0.053	0.819
	B2-10	3.053	2.484	7.932	0.0698	0.258	1623	0.044	0.032	1.112
	D3-3	3.197	2.476	7.497	0.0812	0.232	1985	0.030	0.020	1.012
CO_2 (dry coal)										
	C3-2	7.826	1.359	13.305	0.0130	0.115	2181	0.029	–	1.107
	B2-11	4.678	0.564	13.252	0.0119	0.202	2746	0.055	0.051	0.828
	B2-10	11.136	0.273	13.403	0.0155	0.0743	1622	0.036	0.024	1.112
	D3-3	11.163	1.875	14.712	0.0219	0.0677	1799	0.029	0.019	1.061
CH_4 (wet coal)										
	B2-11	2.237	2.478	13.856	0.0574	0.390	2929	0.051	0.046	0.780
	B2-10	2.499	3.061	13.668	0.0853	0.315	1977	0.035	0.021	1.014
	D3-3	1.462	3.355	13.529	0.108	0.576	2044	0.019	0.0098	1.011

[a] Gas density in cell immediately after dosing into cell (beginning of adsorption step).
[b] Langmuir slope (S_L) and intercept (I_L), see text.
[c] Total porosity (ϕ) and microporosity (ϕ_i) used in unipore and bidisperse numerical models, respectively.

respect to pore volume distribution and therefore adsorption rate models based upon a unimodal pore structure are adequate. The dull (B2-10 and D3-3) samples contain an appreciable proportion of meso/macropores, and therefore dual resistance diffusion models are more appropriate for describing adsorption rate behaviour. Sample B2-11 has a large micropore volume, small mesopore volume, and a large macropore volume, as indicated by mercury porosimetry data, and therefore dual resistance diffusion models are more appropriate for describing this sample's adsorption rate behaviour. The discrepancy in methane adsorption rate behaviour between bright and dull (dry) coals has been previously documented for Australian coals [37]. In the Gamson and Beamish study [37], the difference in dull and bright coal behaviour was explained with the aid of SEM imaging of the coal microstructure.

4.2. High-pressure methane and carbon dioxide adsorption rate data: application of bidisperse models

The bidisperse Ruckenstein [28] model equation (19) as well as the new bidisperse numerical model developed here

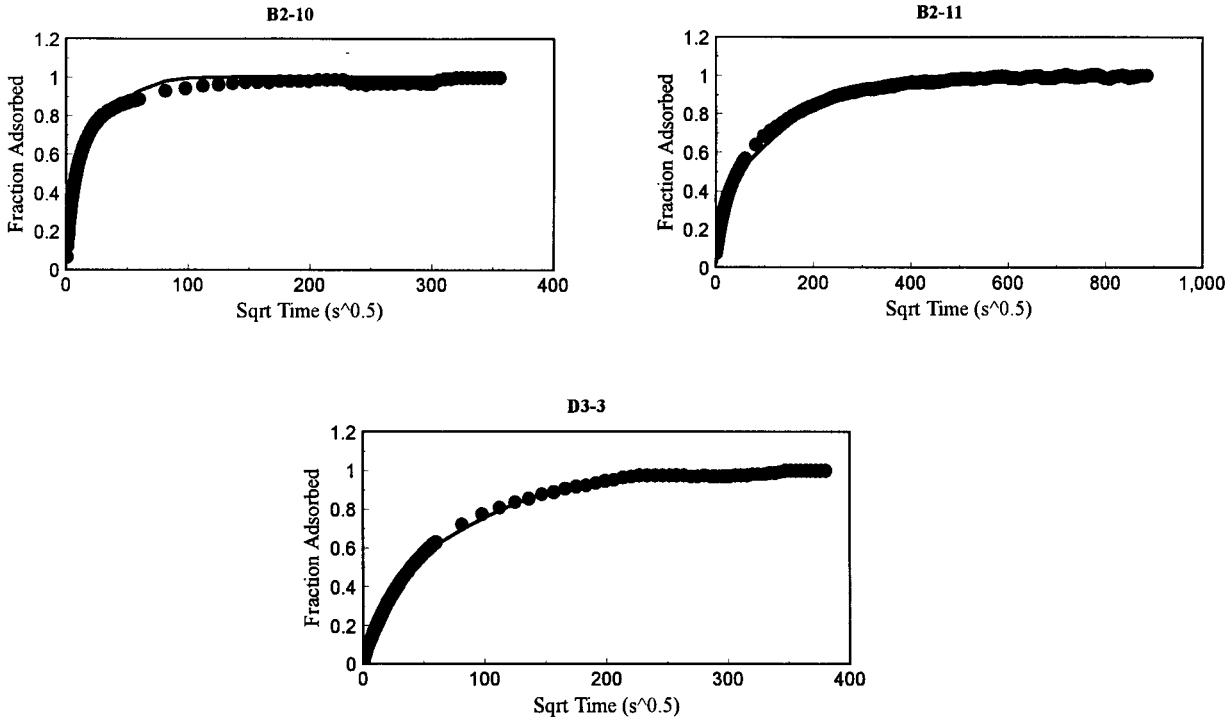

Fig. 8. Bidisperse analytical model fit to − 4 mesh (dry) coal methane adsorption rate data.

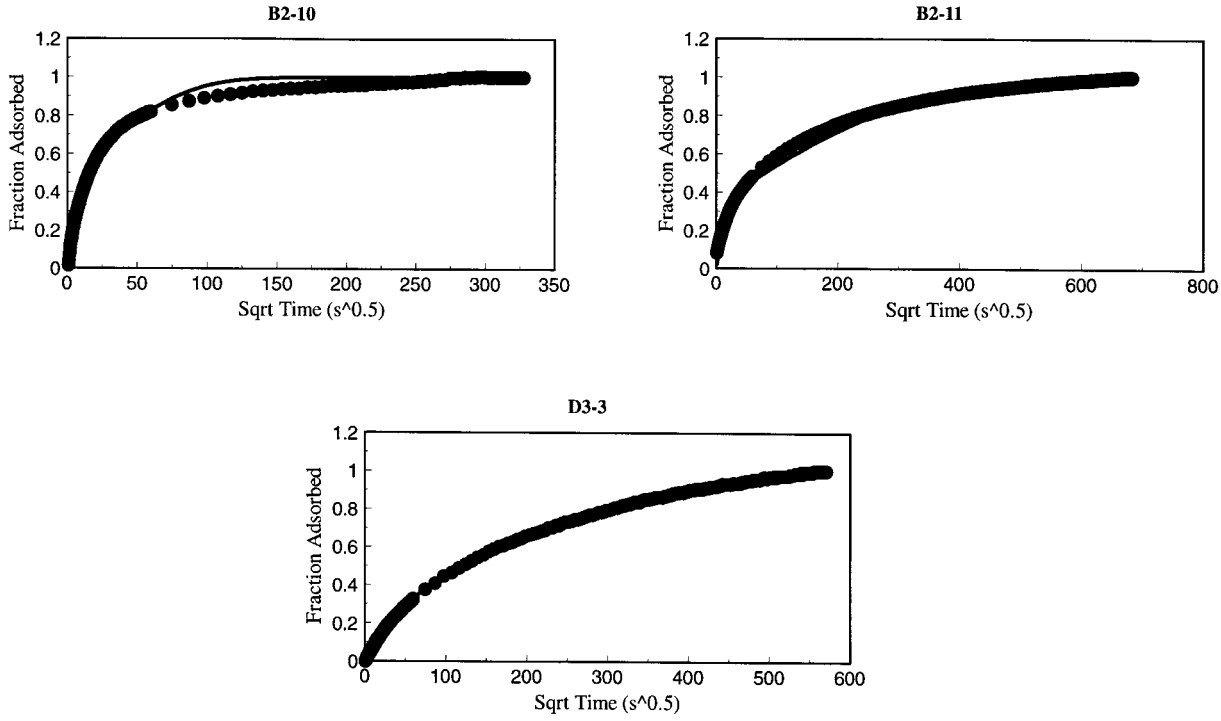

Fig. 9. Bidisperse analytical model fit to − 4 mesh (wet) coal methane adsorption rate data.

were also applied to the high-pressure data (Figs. 8–13). Input to the numerical model is provided in Table 3. Macropore and micropore diffusivities are given in Tables 4 and 5.

Both the analytical and numerical bidisperse models adequately describe the adsorption rate behaviour of the multimodal pore volume coals (B2-10, D3-3, and B2-11) (Figs. 8–13). A transition occurs from macropore-dominated transport at early time, to micropore-dominated transport at later time. This finding is consistent with the

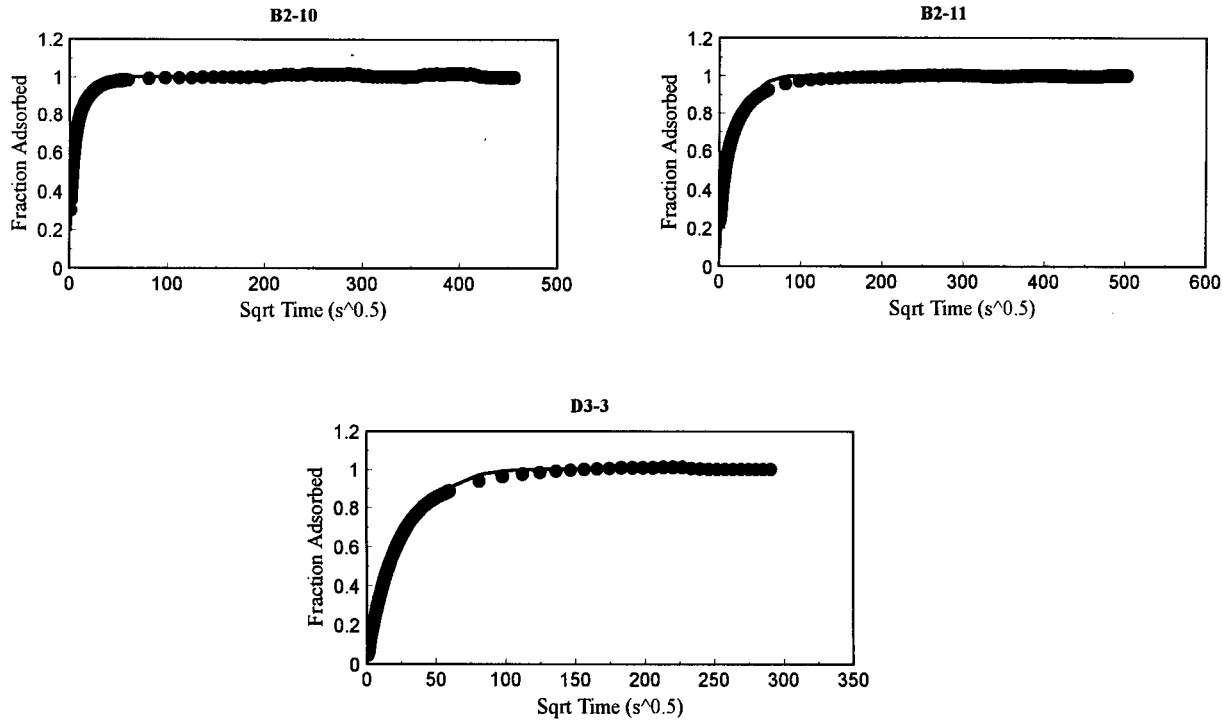

Fig. 10. Bidisperse analytical model fit to − 4 mesh (dry) coal carbon dioxide adsorption rate data.

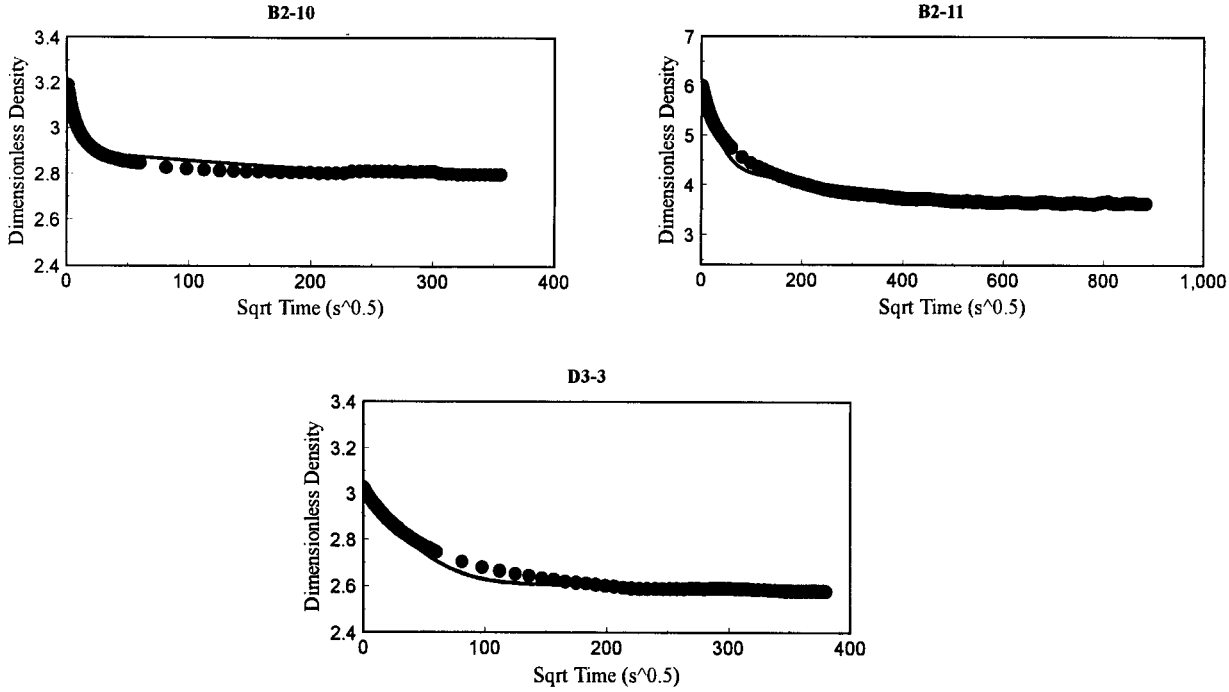

Fig. 11. Bidisperse numerical model fit to − 4 mesh (dry) coal methane adsorption rate data.

findings of Gamson et al. [37] for Australian Bowen Basin coals. The Ruckenstein model [28] methane (macro- and micropore) diffusivities (Table 4) determined from methane adsorption on dry coal are comparable in magnitude (D'_a: 3×10^{-4}–$2 \times 10^{-3}\ s^{-1}$, D'_i: 2×10^{-6}–4×10^{-5}) to those found by Beamish [31] but the macropore diffusivities are somewhat larger than those obtained by Smith and Williams [38]. Ruckenstein macro- and micropore effective diffusivities for methane adsorption on wet coal are generally only slightly smaller than for the dry coals, probably reflecting the small equilibrium moisture content of the Gates coals. The diffusivities for carbon dioxide on dry coal (Table 4) are larger than for methane, which is consistent with the unipore model diffusivities.

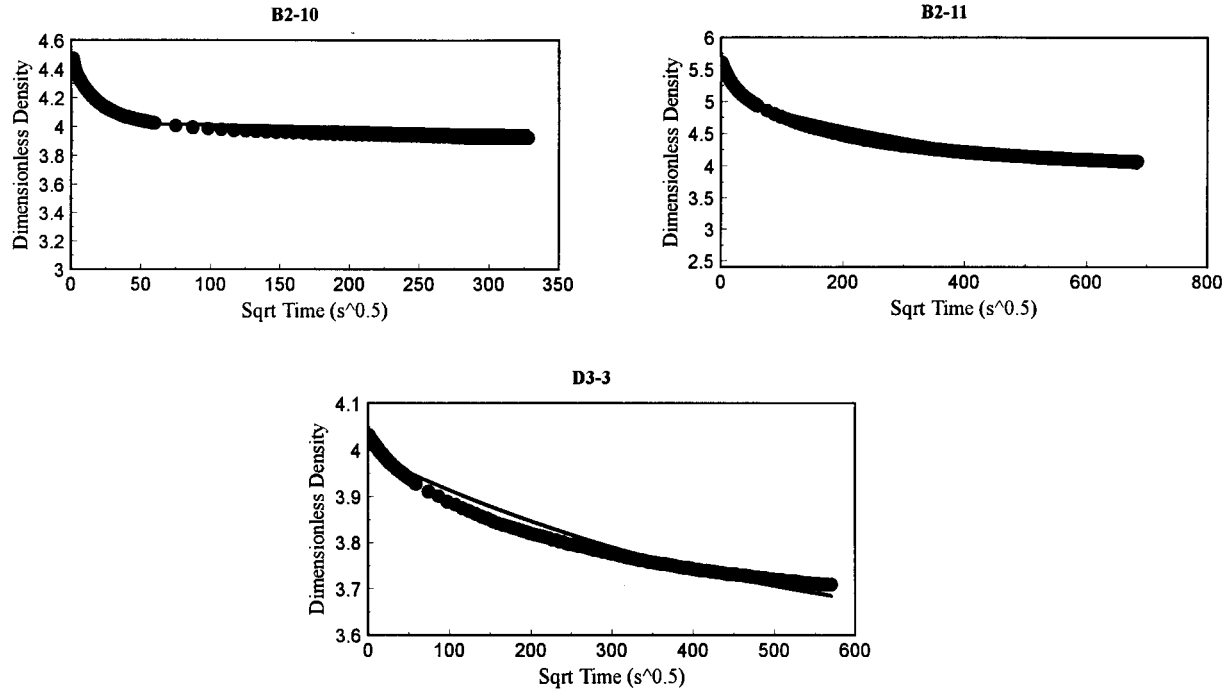

Fig. 12. Bidisperse numerical model fit to − 4 mesh (wet) coal methane adsorption rate data.

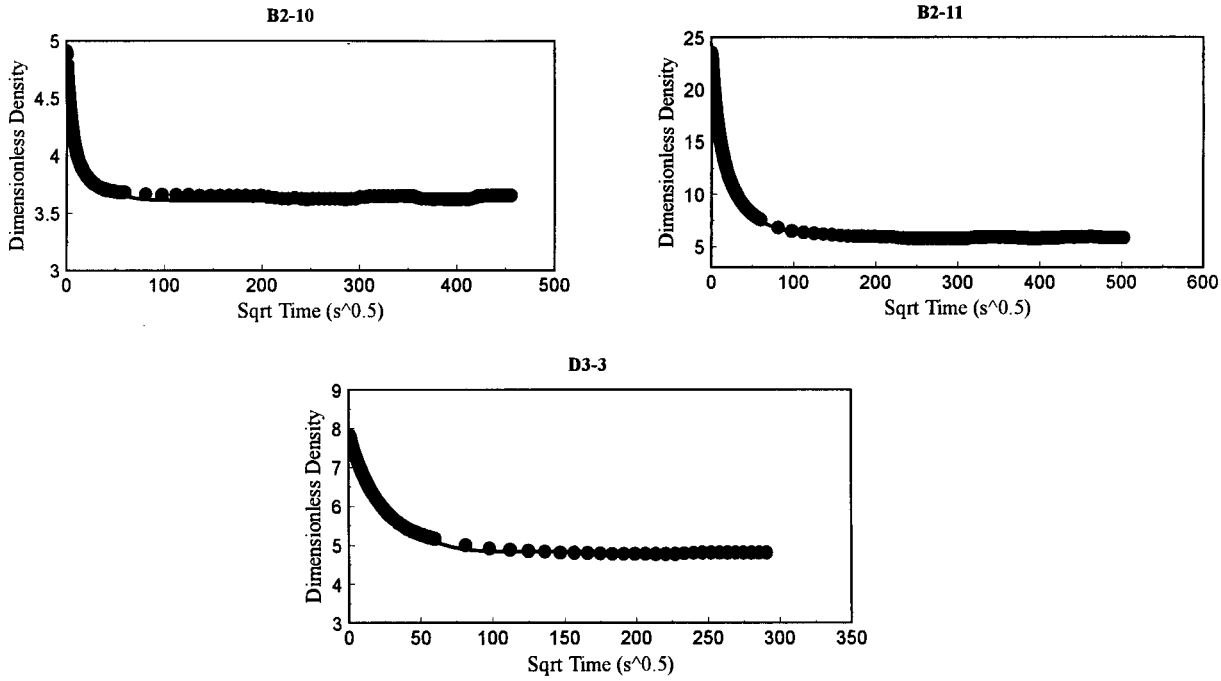

Fig. 13. Bidisperse numerical model fit to − 4 mesh (dry) coal carbon dioxide adsorption rate data.

The numerical model, like the bidsiperse analytical solution, generally captures the adsorption rate behaviour of the multimodel pore volume distribution coals (Figs. 11–13) better than the unipore models. Carbon dioxide diffusivities are much larger than the methane diffusivities. The micropore diffusivities (Table 5) are generally much smaller than the macropore diffusivities, with the exception of the diffusivities obtained for sample D3-3 carbon dioxide data. The anomalous values for sample D3-3 may be the result of a poor fit of the model to the data.

A problem with the bidisperse analytical model is that it is difficult to calculate some physical parameters of the coal from the model parameters. For example, the parameter β is defined in the same way as for the numerical model described above, but the ratio of the diffusivities, α, is unobtainable because the diffusivities obtained in the analytical model solution are not corrected for the effects of (assumed linear) adsorption. As a result, the values of micro- or macroporosity, or their ratios, are unobtainable. However, macroporosity may be obtained from the optimized value of β, α, and the input value of microporosity for the numerical model. For some samples, the estimated macroporosity is much greater (>1 order of magnitude) than the experimentally determined value obtained from nitrogen isotherms and He/Hg pycnometry. This discrepancy may be due to a number of factors including: (1) misfit of the experimental data by the Langmuir model; (2) the assumption of adsorption occurring only in the microporosity of the coal; (3) inaccurate determination of pore volume distributions or porosities; or (4) the assumption of a single average particle size. Bhatia [32], using a random pore model, also found that unrealistically high macroporosities were required to obtain a reasonable fit to the adsorption rate data of Nandi and Walker [19]. Bhatia [32] interpreted the unrealistic calculated macroporosities to be (possibly) due to a nonrandom distribution of macropores throughout the solid.

Table 4
Bidisperse analytical (Ruckenstein) model parameters for adsorption rate data-isotherm pressure step 2

Sample	CH_4 on dry coal		CH_4 on moisture-equilibrated coal		CO_2 on dry coal	
	D'_a[a] (s^{-1})	D'_i[b] (s^{-1})	D'_a (s^{-1})	D'_i (s^{-1})	D'_a (s^{-1})	D'_i (s^{-1})
C3-2	–	–	–	–	–	–
B2-11	3×10^{-4}	2×10^{-6}	3×10^{-4}	1×10^{-6}	5×10^{-3}	6×10^{-5}
D3-3	2×10^{-4}	6×10^{-6}	5×10^{-5}	1×10^{-6}	6×10^{-4}	4×10^{-5}
B2-10	2×10^{-3}	4×10^{-5}	7×10^{-4}	2×10^{-5}	9×10^{-3}	2×10^{-4}

[a] $D'_a = (D_a/R_a^2)(\phi_a/(\phi_a + S_a H_a))$.
[b] $D'_i = D_i/R_i^2(\phi_i/(\phi_i + S_i H_i))$.

Table 5
Bidisperse numerical model parameters for adsorption rate data-isotherm pressure step 2

Sample	CH_4 on dry coal		CH_4 on moisture-equilibrated coal		CO_2 on dry coal	
	D_a/R_a^2 (s^{-1})	D_i/R_i^2 (s^{-1})	D_a/R_a^2 (s^{-1})	D_i/R_i^2 (s^{-1})	D_a/R_a^2 (s^{-1})	D_i/R_i^2 (s^{-1})
C3-2	–	–	–	–	–	–
B2-11	3×10^{-5}	5×10^{-6}	1×10^{-4}	3×10^{-6}	6×10^{-3}	2×10^{-3}
D3-3	2×10^{-5}	5×10^{-8}	5×10^{-4}	1×10^{-5}	1×10^{-3}	3×10^{-3}
B2-10	7×10^{-4}	5×10^{-6}	2×10^{-4}	3×10^{-7}	3×10^{-2}	4×10^{-3}

4.3. Low-pressure carbon dioxide adsorption rate data: application of bidisperse models

Carbon dioxide adsorption rate data collected for the −4 mesh coals at low pressure (<127 kPa) (Fig. 14) showed similar trends to the high-pressure methane and carbon dioxide data described above. The unipore model was inadequate for modeling adsorption rate data for the banded bright or dull coals.

The carbon dioxide macropore and micropore effective diffusivities (Table 6) are smaller than for the high-pressure data, which is anticipated because the high-pressure analyses were performed at a higher temperature (303 K) than the low-pressure analyses (273 K).

4.4. Methane and carbon dioxide adsorption rate data: effect of gas pressure

To determine the effect of pressure upon calculated diffusivities, model (numerical and analytical) diffusivities were determined from several pressure steps of the adsorption isotherm. Methane diffusivities determined from the unipore analytical and numerical model are plotted against equilibrium adsorption pressure in Fig. 15. One set of diffusivity values, obtained from desorption, is also plotted and is consistent with the trend of adsorption step diffusivities with pressure. The unipore diffusivities exhibit a strong dependence upon adsorption pressure. Although some scatter in the data exists, the numerical model diffusivities decrease with pressure, whereas the analytical model diffusivities increase with pressure. The increase in analytical model diffusivities with pressure may be due to the nonlinearity of the isotherm as suggested by previous authors [24], but the decrease in numerical diffusivities, which have been corrected for the effects of nonlinear adsorption, with pressure may be due to the mechanism of gaseous diffusion.

The mechanism of methane gas diffusion in the Gates coals appears to be bulk diffusion. In an earlier study, Smith and Williams [20] have shown that the mechanisms of gaseous methane diffusion in bituminous coal vary with pressure. In particular, they (opt. cit.) note that the mechanism of diffusion changes from Knudsen type diffusion below a pressure of about 0.2 MPa to bulk diffusion at higher pressures, which they interpret to be due to the decrease in mean free path of the methane molecule with gas pressure. The decrease in the numerical model diffusivities, which are corrected for the effects of adsorption, with gas pressure is therefore consistent with a mechanism of bulk diffusion in the Gates coals.

The Ruckenstein (analytical) model diffusivities for low-pressure 273 K carbon dioxide adsorption obtained for sample B2-10 are plotted versus pressure in Fig. 16. For this sample, both the macropore and the micropore diffusivities increase with pressure, although the micropore diffusivities are more strongly dependent upon pressure. The increase in diffusivity may (again) be due to the nonlinearity of the isotherm. If so, the results suggest that significant adsorption is occurring in both the meso/macroporosity and the microporosity, which contradicts the assumptions used in the bidisperse numerical model. Further work is required to resolve this issue.

4.5. Implications for reservoir characterization and modeling

The above results have demonstrated that two factors

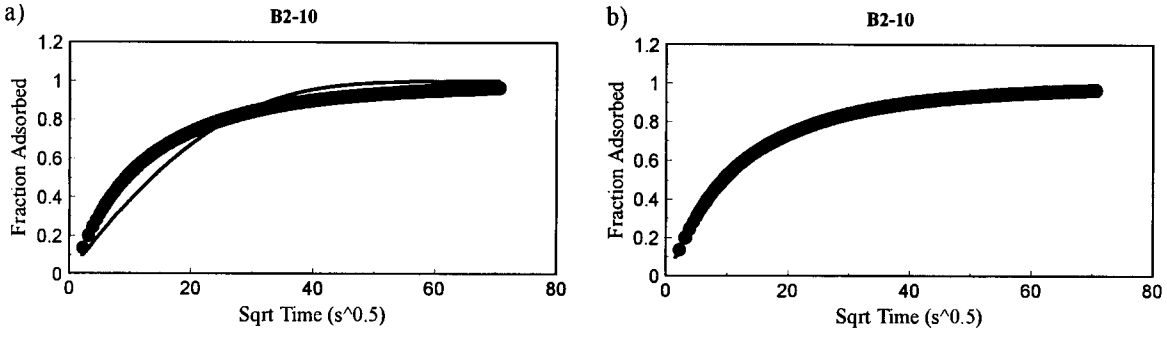

Fig. 14. Analytical model fit to −4 mesh (dry) coal low-pressure carbon dioxide adsorption rate data: (a) unipore model; and (b) bidisperse model.

Table 6
Bidisperse analytical (Ruckenstein) model parameters for sample B2-10 adsorption rate data

Pressure (mmHg)	D'^{a}_{a} (s^{-1})	D'^{b}_{i} (s^{-1})
17.428	5×10^{-4}	4×10^{-5}
40.9583	6×10^{-4}	4×10^{-5}
264.264	7×10^{-4}	4×10^{-5}
310.911	7×10^{-4}	4×10^{-5}
359.419	7×10^{-4}	5×10^{-5}
728.509	1×10^{-3}	6×10^{-5}
786.327	1×10^{-3}	8×10^{-5}
845.385	1×10^{-3}	1×10^{-4}
888.567	1×10^{-3}	1×10^{-4}

[a] $D'_a = D_a/R_a^2(\phi_a/(\phi_a + S_aH_a))$.
[b] $D'_i = D_i/R_i^2(\phi_i/(\phi_i + S_iH_i))$.

have a strong effect upon the transport of methane and carbon dioxide gas through the matrix of coals: pore volume distribution and gas pressure. Some current techniques for determining lost gas for canister desorption tests [6] assume that a single diffusion coefficient, independent of gas concentration or pressure, is adequate for the description of coal matrix gas transport. The current study shows that, because the coal pore volume distribution is a function of coal composition, a single parameter (diffusion coefficient or diffusivity) matrix gas diffusion model may be inadequate for describing adsorption rate behaviour for all coal sampled from a reservoir. Reservoirs are not entirely homogeneous with respect to organic and mineral composition, or organic and mineral content. Thus, a single parameter diffusivity model may lead to error (underestimate) in lost gas determination, and hence total in-situ gas content for a coal reservoir. This study shows that the diffusivity errors may be up to an order of magnitude if a single parameter model is used instead of dual resistance models. In a study by Mavor and Pratt [39], the Ruckenstein bidisperse model and the Direct Method [6], which uses an estimate of a single diffusivity value, were applied to gas canister desorption data. For most samples (four out of five) the two models gave similar estimates of lost gas, and hence total gas content, but the differences between the two estimates became greater as the lost gas content increased [39]. It is anticipated, based on the adsorption rate data given above, that dull coals, or coals with a significant fraction of meso- and macroporosity, would have a greater percentage of lost gas than coals with less macro/mesoporosity. Lost gas determinations obtained using single diffusivity models may therefore have a greater error for coals of particular composition, which would create error in total gas content estimates for heterogeneous reservoirs. Additionally, because the pore volume distribution of coals is known to be a function of rank [27], or thermal maturity of the coal, models utilizing single diffusivity values may be adequate in the determination of lost gas only for certain rank ranges.

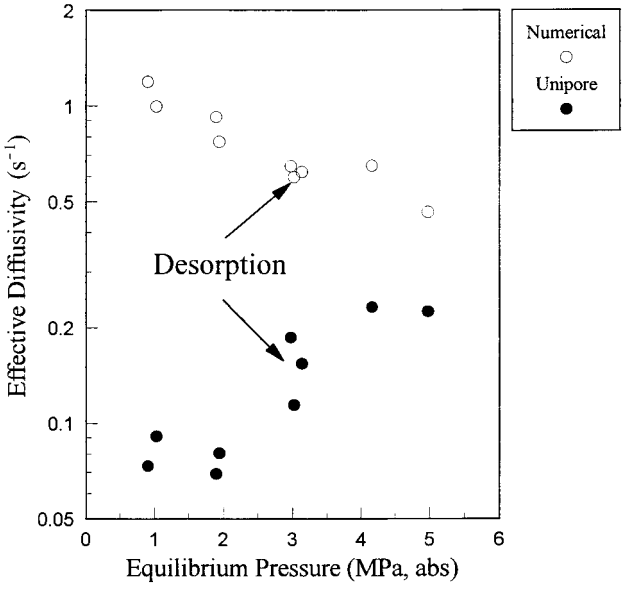

Fig. 15. Methane effective diffusivities vs. pressure for sample C3-2.

The pressure-dependence exhibited by the numerical and analytical model diffusivities has important implications for the determination of diffusion parameters during adsorption isotherm collection (as shown above), but also for the use of diffusivities in reservoir production modeling. The pressure-dependence of diffusivities is particularly important if adsorption rate data are obtained over a large pressure step which is often the case in desorption measurements. The assumption of a linear isotherm, as with the Ruckenstein model [28], may lead to erroneous values of diffusivity for coal. We suggest that the pressure-dependence of diffusivities should be ascertained prior to the application of diffusion models for the determination of lost gas calculations [6], as well as for reservoir simulators, where coal cleat and matrix fluid pressure varies with time during production. The diffusivity would be expected to vary during production and production models based upon constant diffusivity values may be in error. The impact of pressure and concentration upon diffusivities upon production forecasting requires study.

5. Conclusions

1. Carbon dioxide diffusivities are generally larger than methane diffusivities obtained for dry coal. Wet coal methane diffusivities are generally smaller than methane diffusivities determined for dry coals.
2. Bright coals have a uniform micropore structure and their adsorption rate data are adequately modeled using the classic unipore analytical solution or the proposed numerical model. Dull or banded coals have a more complicated pore structure, and are adequately modeled with diffusion models that incorporate a bidisperse pore volume distribution. Close examination of numerical model optimized parameters suggest that some of the assumptions of the bidisperse model may be invalid.

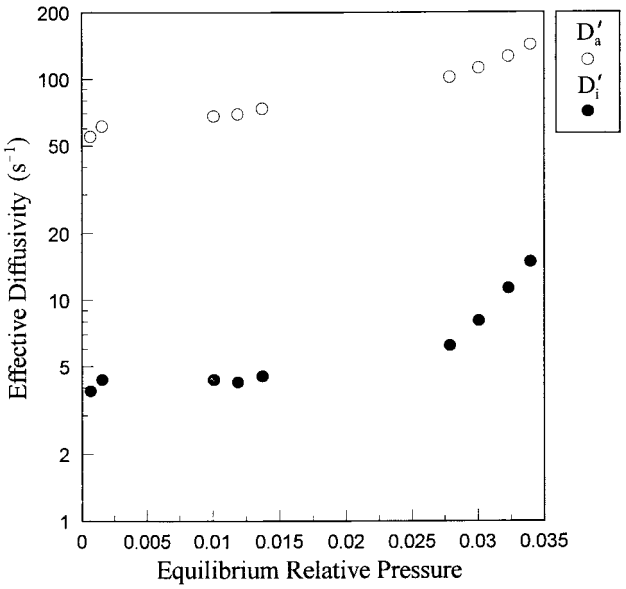

Fig. 16. Low-pressure (273 K) carbon dioxide macropore and micropore effective diffusivities vs. pressure for sample B2-10.

3. Methane effective diffusivities obtained using the unipore analytical and numerical solutions are dependent upon adsorption pressure. The pressure dependence of the numerical model diffusivities is consistent with a bulk gaseous diffusion mechanism. Carbon dioxide diffusivities obtained using low-pressure (<127 kPa) 273 K isotherm and the Ruckenstein model also exhibit a pressure dependence. These findings may have important implications for gas content determination and reservoir simulations, although further study is required.

Acknowledgements

Funding for this study was provided by NSERC grant A-7337 to R.M. Bustin. The authors would like to thank T.J. Pratt and Dr D.M. Smith for their careful review of this manuscript.

Appendix A. Discretization of macropore transport equation

The (dimensionless) macropore transport equation is:

$$\frac{1}{\eta^2}\frac{\partial}{\partial\eta}\left(\eta^2\frac{\partial\rho_{D_a}}{\partial\eta}\right)=\frac{\partial\rho_{D_a}}{\partial\tau}+\beta\frac{\partial\rho_{D_i}}{\partial\gamma}\Big|_{\gamma=1}. \tag{A.1}$$

A.1. Discretization of equations

Eq. (A.1) may be written in the following generalized form:

$$\nabla\cdot q-\frac{\partial\rho_{D_a}}{\partial\tau}-g_i=0$$

where q is the (dimensionless) flux of gas in the macroporosity, and g_i is the macropore to microporous matrix mass flow rate. Following the integrated finite difference approach [34], this equation may be spatially integrated over a small subregion of the macrosphere domain:

$$\int_V(\nabla\cdot q)\,\mathrm{d}V-\frac{\partial}{\partial\tau}\int_V\rho_{D_a}\,\mathrm{d}V-\int_V g_i\,\mathrm{d}V=0. \tag{A.2}$$

In the current problem, the finite subvolume is a spherical shell within the macrosphere (Fig. 1). In addition, we have assumed a spherically symmetrical system. The spherical volume element is:

$$\mathrm{d}V=\eta^2\,\mathrm{d}\eta\,\mathrm{d}\theta\sin\Phi\,\mathrm{d}\Phi,$$

where η is the radial coordinate, θ the azimuth angle, and Φ the angle of elevation. Substituting the divergence term (radial coordinates) from the left hand side of Eq. (A.1) and the definition of the spherical volume element into (A.2):

$$\begin{aligned}&\int_V\frac{1}{\eta^2}\frac{\partial}{\partial\eta}\left(\eta^2\frac{\partial\rho_{D_a}}{\partial\gamma}\right)\eta^2\,\mathrm{d}\eta\,\mathrm{d}\theta\sin\Phi\,\mathrm{d}\Phi\\&-\frac{\partial}{\partial\tau}\int_V\rho_{D_a}\eta^2\,\mathrm{d}\eta\,\mathrm{d}\theta\sin\Phi\,\mathrm{d}\Phi\\&-\int_V g_i\,\mathrm{d}\eta\,\mathrm{d}\theta\sin\Phi\,\mathrm{d}\Phi=0.\end{aligned} \tag{A.3}$$

The discretization volume is an interior spherical subshell extending from $\eta_{I-1/2}$ to $\eta_{I+1/2}$ centred on node I. Eq. (A.3) thus becomes:

$$\begin{aligned}&\int_0^{\pi}\int_0^{2\pi}\int_{\eta_{I-1/2}}^{\eta_{I+1/2}}\frac{1}{\eta^2}\frac{\partial}{\partial\eta}\left(\eta^2\frac{\partial\rho_{D_a}}{\partial\eta}\right)\eta^2\,\mathrm{d}\eta\,\mathrm{d}\theta\sin\Phi\,\mathrm{d}\Phi\\&-\frac{\partial}{\partial\tau}\int_0^{\pi}\int_0^{2\pi}\int_{\eta_{I-1/2}}^{\eta_{I+1/2}}\rho_{D_a}\eta^2\,\mathrm{d}\eta\,\mathrm{d}\theta\sin\Phi\,\mathrm{d}\Phi\\&-\int_0^{\pi}\int_0^{2\pi}\int_{\eta_{iI-1/2}}^{\eta_{I+1/2}}g_i\eta^2\,\mathrm{d}\eta\,\mathrm{d}\theta\sin\Phi\,\mathrm{d}\Phi\\&=0.\end{aligned}$$

Carrying out the integrations:

$$\begin{aligned}&4\pi\eta_{I+1/2}^2\left[\frac{\partial\rho_{D_a}}{\partial\eta}\Big|_{I+1/2}\right]-4\pi\eta_{I-1/2}^2\left[\frac{\partial\rho_{D_a}}{\partial\eta}\Big|_{I-1/2}\right]\\&-\frac{4}{3}\pi\left[\eta_{I+1/2}^3-\eta_{I-1/2}^3\right]\frac{\partial\rho_{D_a}}{\partial\tau}-\frac{4}{3}\pi\left[\eta_{I+1/2}^3-\eta_{I-1/2}^3\right]g_i=0.\end{aligned} \tag{A.4}$$

The spatial derivatives may be approximated by second order central differences, and the time derivative may be approximated by a backward difference. In addition we may define a geometric term (G) at the $\eta_{I-1/2}$ and $\eta_{I+1/2}$ spherical interface and the discretized subshell volume as:

$$G(I-1/2)=4\pi\eta_{I-1/2}^2/(\eta_I-\eta_{I-1}),$$

$$G(I+1/2) = 4\pi\eta_{I+1/2}^2/(\eta_{I+1}-\eta_I),$$

$$\mathrm{Vol}(I) = \frac{4}{3}\pi[\eta_{I+1/2}^3 - \eta_{I-1/2}^3].$$

Substituting these definitions into Eq. (A.4) yields the discretized form of Eq. (A.1) for the *I*th interior spherical element:

$$G(I+1/2)(\rho_{D_aI+1}-\rho_{D_aI}) - G(I-1/2)(\rho_{D_aI}-\rho_{D_aI-1}) - \mathrm{Vol}(I)\frac{\rho_{D_aI}-\rho_{D_aI}^{\vee}}{\Delta\tau} - \mathrm{Vol}(I)g_i = 0, \quad (A.5)$$

$$-\Delta\tau G(I+1/2)(\rho_{D_aI+1}-\rho_{D_aI}) + \Delta\tau G(I-1/2)(\rho_{D_aI} - \rho_{D_aI-1}) + \Delta\tau\mathrm{Vol}(I)g_i + \mathrm{Vol}(I)\rho_{D_aI} = \mathrm{Vol}(I)\rho_{D_aI}^{\vee}$$

where superscript $\vee$ refers to the previous timestep. Eq. (A.5) may be reduced to the following form:

$$A_{I-1}\rho_{D_aI-1} + B_I\rho_{D_aI} + C_{I+1}\rho_{D_aI+1} = \rho_{D_aI}^{\vee} - \Delta\tau g_i. \quad (A.6)$$

Appendix B. Discretization of micropore transport equation

The (dimensionless) micropore transport equation is:

$$\frac{\alpha}{\gamma^2}\frac{\partial}{\partial\gamma}\left(\gamma^2\frac{\partial\rho_{D_i}}{\partial\gamma}\right) = \frac{\partial}{\partial\tau}\left(\rho_{D_i} + \frac{C_s}{\rho_o\phi_i}\right) \quad (B.1)$$

or

$$\frac{\alpha}{\gamma^2}\frac{\partial}{\partial\gamma}\left(\gamma^2\frac{\partial\rho_{D_i}}{\partial\gamma}\right) = \frac{\partial\Theta}{\partial\tau}$$

where $\Theta = \rho_{D_i} + (C_S/\rho_o\phi_i)$.

B.1. Discretization of equations

Eq. (B.1) may be written in the following generalized form:

$$\nabla\cdot q - \frac{\partial\Theta}{\partial\tau} = 0$$

where q is the (dimensionless) flux of gas in the microporosity. Applying the integrated finite difference approach, this equation may be spatially integrated over a small subregion of the microsphere domain:

$$\int_V(\nabla\cdot q)\,\mathrm{d}V - \frac{\partial}{\partial\tau}\int_V\Theta\,\mathrm{d}V = 0. \quad (B.2)$$

In the current problem, the finite subvolume is a spherical shell within the microsphere (Fig. 1). In addition, we have assumed a spherically symmetrical system. The spherical volume element is:

$$\mathrm{d}V = \gamma^2\,\mathrm{d}\gamma\,\mathrm{d}\theta\sin\Phi\,\mathrm{d}\Phi$$

where γ is the radial coordinate, θ the azimuth angle, and Φ the angle of elevation. Substituting the divergence term (radial coordinates) from the left-hand side of Eq. (B.1) and the definition of the spherical volume element into (B.2):

$$\int_V\frac{\alpha}{\gamma^2}\frac{\partial}{\partial\gamma}\left(\gamma^2\frac{\partial\rho_{D_i}}{\partial\gamma}\right)\gamma^2\,\mathrm{d}\gamma\,\mathrm{d}\theta\sin\Phi\,\mathrm{d}\Phi - \frac{\partial}{\partial\tau}\int_V\Theta\gamma^2\,\mathrm{d}\gamma\,\mathrm{d}\theta\sin\Phi\,\mathrm{d}\Phi = 0. \quad (B.3)$$

The discretization volume is an interior spherical subshell extending from $\gamma_{I-1/2}$ to $\gamma_{I+1/2}$ centred on node *I*. Eq. (B.3) thus becomes:

$$\int_0^{\pi}\int_0^{2\pi}\int_{\gamma_{I-1/2}}^{\gamma_{I+1/2}}\frac{\alpha}{\gamma^2}\frac{\partial}{\partial\gamma}\left(\gamma^2\frac{\partial\rho_{D_i}}{\partial\gamma}\right)\gamma^2\,\mathrm{d}\gamma\,\mathrm{d}\theta\sin\Phi\,\mathrm{d}\Phi - \frac{\partial}{\partial\tau}\int_0^{\pi}\int_0^{2\pi}\int_{\gamma_{I-1/2}}^{\gamma_{I+1/2}}\Theta\gamma^2\,\mathrm{d}\gamma\,\mathrm{d}\theta\sin\Phi\,\mathrm{d}\Phi = 0.$$

Carrying out the integrations and assuming a constant α:

$$\alpha 4\pi\gamma_{I+1/2}^2\left[\left.\frac{\partial\rho_{D_i}}{\partial\gamma}\right|_{I+1/2}\right] - \alpha 4\pi\gamma_{I-1/2}^2\left[\left.\frac{\partial\rho_{D_i}}{\partial\gamma}\right|_{I-1/2}\right] - \frac{4}{3}\pi\left[\gamma_{I+1/2}^3 - \gamma_{I-1/2}^3\right]\frac{\partial\Theta}{\partial\tau} = 0. \quad (B.4)$$

The spatial derivatives may be approximated by second order central differences, and the time derivative may be approximated by a backward difference. In addition we may define a geometric term (G) at the $\gamma_{I-1/2}$ and $\gamma_{I+1/2}$ spherical interface and the discretized subshell volume as:

$$G(I-1/2) = 4\pi\gamma_{I-1/2}^2\alpha/(\gamma_I - \gamma_{I-1}),$$

$$G(I+1/2) = 4\pi\gamma_{I+1/2}^2\alpha/(\gamma_{I+1} - \gamma_I),$$

$$\mathrm{Vol}(I) = \frac{4}{3}\pi\left[\gamma_{I+1/2}^3 - \gamma_{I-1/2}^3\right].$$

Substituting these definitions into Eq. (B.4) yields the discretized form of Eq. (B.1) for the *i*th interior spherical element:

$$G(I+1/2)(\rho_{D_iI+1}-\rho_{D_iI}) - G(I-1/2)(\rho_{D_iI}-\rho_{D_iI-1}) + \mathrm{Vol}(I)\frac{\Theta_I - \Theta_I^{\vee}}{\Delta\tau} = 0 \quad (B.5)$$

$$\Delta\tau G(I+1/2)(\rho_{D_iI+1}-\rho_{D_iI})-\Delta\tau G(I-1/2)(\rho_{D_iI}-\rho_{D_iI-l})+\mathrm{Vol}(I)\Theta_I=\mathrm{Vol}(I)\Theta_I^{\vee}$$

where superscript $\vee$ refers to the previous timestep.

Eq. (B.5) may be reduced to the following form:

$$A_{I-1}\rho_{D_iI-1}+B_I\rho_{D_iI}+C_{I+1}\rho_{D_iI+1}+\Theta_I=\Theta_I^{\vee}. \quad \text{(B.6)}$$

Appendix C. Linearization of discretized equations and solution procedure

If the nonlinear Langmuir isotherm equation is used in the dimensionless storage term Θ_I in equations of the form (B.6), the resulting equations are nonlinear in form. The Newton − Raphson technique is used to linearize the equations. The solution of the micropore transport equation, using the example of Eq. (B.6) for the Ith node, is as follows:

1. At each new iteration $(\nu+1)$ the approximations $\rho_{D_i}^{(\nu+1)}=\rho_{D_i}^{(\nu)}+\Delta\rho_{D_i}^{(\nu)}$ and $\Theta(\rho_{D_i}^{(\nu)})+(\partial\Theta(\rho_{D_i}^{(\nu)})/\partial\rho_{D_i})\Delta\rho_{D_i}^{(\nu)}$ are substituted into equations of the form (B.6).
2. The resulting equations are of the form:

$$A_{I-1}\Delta\rho_{D_iI-1}^{(\nu)}+\left\{B_I+\Theta'(\rho_{D_iI}^{(\nu)})\right\}\Delta\rho_{D_iI}^{(\nu)}+C_{I+1}\Delta\rho_{D_iI+1}^{(\nu)}=\Theta_I^{\nu}-\left\{\Theta_I^{(\nu)}+A_{I-1}\rho_{D_iI-1}^{(\nu)}+B_I\rho_{D_iI}^{(\nu)}+C_{I+1}\rho_{D_iI+1}^{(\nu)}\right\}$$

or

$$A_{I-1}\Delta\rho_{D_iI-1}^{(\nu)}+\left\{B_I+\Theta'(\rho_{D_iI}^{(\nu)})\right\}\Delta\rho_{D_iI}^{(\nu)}+C_{I+1}\Delta\rho_{D_iI+1}^{(\nu)}=R_I,$$

where R_I is the residual.
3. The resulting set of linearized equations, with the coefficients forming a tridiagonal matrix, are solved using a direct solver routine. The resulting $\Delta\rho_{D_iI}$ are then used in the latest approximation to ρ_{D_iI}.
4. The above procedures are repeated until the residuals of the equations in procedure (2) are minimized.

References

[1] King GR, Ertekin T, Schwerer FC. SPE Formation Evaluation 1986:165.
[2] Kolesar JE, Ertekin T. In: Proceedings of the Society of Petroleum Engineers Unconventional Gas Technology Symposium, Louisville, Kentucky, 18–21 May 1986, Houston, Texas, pp. 289–314.
[3] Sawyer WK, Zuber MD, Kuuskra VA, Horner DM. In: Proceedings of the 1987 Coalbed Methane Symposium, Tuscaloosa, 16–19 November 1987, pp. 295–307.
[4] Reid GW, Towler BF, Harris HG. Paper SPE 24360 presented at the SPE Rocky Mountain Regional Meeting, Casper, Wyoming, 18–21 May 1992, pp. 425–432.
[5] Harpalani S. Personal communication, 1996.
[6] McLennan JD, Schafer PS, Pratt TJ. A guide to determining coalbed gas content. Gas Research Institute Report No. GRI-94/0396, Chicago, Illinois, 1995.
[7] Mavor MJ, Pratt TJ, Nelson CR. In: Proceedings of the 1995 Intergas Symposium, Tuscaloosa, 14–20 May 1995, pp. 379–388.
[8] Unsworth JF, Fowler CS, Jones LF. Fuel 1989;68:18.
[9] Clarkson CR, Bustin RM. Fuel 1996;75:1483.
[10] Lamberson MN, Bustin RM. AAPG Bull 1993;77:2062.
[11] Beamish BB, Crosdale PJ. In: Proceedings of the International Symposium cum Workshop on Management and Control of High Gas Emission and Outbursts, Wollongong, 20–24 March 1995, pp. 353–361.
[12] Bustin RM, Clarkson C, Levy J. In: Proceedings of the 29th Newcastle Symposium, “Advances in the Study of the Sydney Basin”, University of Newcastle, 1995, pp. 22–28.
[13] Mavor MJ, Owen LB, Pratt TJ. Paper SPE 20728. Presented at the 65th Annual Technical Conference of the Society of Petroleum Engineers, New Orleans, Louisiana, 23–26 September 1990, pp. 1–14.
[14] Ciembroniewicz A, Marecka A. Fuel 1993;72:405.
[15] Marecka A. Coal Sci 1995:23.
[16] Greaves KH, Owen LB, McLennan JD. In: Proceedings of the 1993 International Coalbed Methane Symposium, Tuscaloosa, 17–21 May 1993, pp. 151–160.
[17] Gunter WD, Wiwchar B, Perkins EH. Mineralogy and Petrology 1997;59:140.
[18] Sevenster PG. Fuel 1959;38:403.
[19] Nandi SP, Walker Jr PL. Fuel 1970;49:309.
[20] Smith DM, Williams FL. Society of the Petroleum Engineers Journal 1984;24:529.
[21] Crosdale PJ, Beamish BB. In: Proceedings of the International Symposium cum Workshop on Management and Control of High Gas Emissions and Outbursts, Wollongong, 20–24 March 1995, pp. 363–367.
[22] Crank J. Mathematics of diffusion. London: Oxford University Press, 1975.
[23] Smith DM, Williams FL. Fuel 1984;63:251.
[24] Nandi SL, Walker Jr PL. Fuel 1975;54:81.
[25] Bielicki RJ, Perkins JH, Kissell FN. US Bureau of Mines RI 7697, 1972, 12p.
[26] Smith DM, Keller JF. Ind Engng Chem Fundam 1985;24:497.
[27] Gan H, Nandi SP, Walker Jr PL. Fuel 1972;51:271.
[28] Ruckenstein E, Vaidyanathan AS, Youngquist GR. Chem Engng Sci 1971;26:1305.
[29] Ma YH, Lee TY. AIChE J 1976;22:147.
[30] Lee LK. AIChE J 1978;24:531.
[31] Beamish BB. PhD thesis, The University of Auckland, 1996.
[32] Bhatia SK. AIChE J 1987;33:1707.
[33] Langmuir I. J Am Chem Soc 1918;40:1361.
[34] Narasimhan TN, Witherspoon PA. Water Resour Res 1976;12:57.
[35] Kolesar JE, Ertekin T, Obut ST. SPE Formation Evaluation 1990;:81.
[36] Press WH, Teukolsky SA, Vettering WT, Flannery BP. Numerical recipes in FORTRAN: the art of scientific computing. 2. Cambridge: Cambridge University Press, 1994.
[37] Gamson PD, Beamish B, Johnson D. In: Gayer R, Harris I, editors. Coalbed methane and coal geology, 109. Geological Society of America, 1996. pp. 165–179.
[38] Smith DM, Williams FL. Fuel 1984;63:256.
[39] Mavor MJ, Pratt TJ. Improved methodology for determining total gas content. Volume II: comparative evaluation of the accuracy of gas-in-place estimates and review of lost gas models’. Gas Research Institute Report No. GRI-94/0429, Chicago, Illinois, 1996.